748 K (475 °C) Embrittlement of Duplex Stainless Steel: Effect on Microstructure and Fracture Behavior

CEM ÖRNEK, M.G. BURKE, T. HASHIMOTO, and D.L. ENGELBERG

22Cr-5Ni duplex stainless steel (DSS) was aged at 748 K (475 °C) and the microstructure development correlated to changes in mechanical properties and fracture behavior. Tensile testing of aged microstructures confirmed the occurrence of 748 K (475 °C) embrittlement, which was accompanied by an increase of strength and hardness and loss of toughness. Aging caused spinodal decomposition of the ferrite phase, consisting of Cr-enriched α'' and Fe-rich α' and the formation of a large number of *R*-phase precipitates, with sizes between 50 and 400 nm. Fracture surface analyses revealed a gradual change of the fracture mode from ductile to brittle delamination fracture, associated with slip incompatibility between ferrite and austenite. Ferrite became highly brittle after 255 hours of aging, mainly due to the presence of precipitates, while austenite was ductile and accommodated most plastic strain. The fracture mechanism as a function of 748 K (475 °C) embrittlement is discussed in light of microstructure development.

DOI: 10.1007/s11661-016-3944-2

I. INTRODUCTION

DUPLEX stainless steels (DSSs) are highly corrosion and stress corrosion cracking (SCC) resistant materials with good mechanical properties. The microstructure consists of ferrite (δ) and austenite (γ), usually in a balanced ratio, and is tailored to provide excellent electrochemical behavior with good mechanical strength, ductility, and fracture toughness. DSSs have been successfully used in many critical applications, including petrochemical, off-shore, marine, and nuclear.[1–3] The mechanical strength and toughness derive from their chemical composition and small grain size, typically on the order of 5 to 10 μm, and the balanced ratio of ferrite and austenite, resulting in a synergism in which both phases support each other. Mechanical properties and the SCC behavior are influenced by the ferrite-to-austenite ratio.[4] Strength and creep resistance are usually governed by the ferrite, whereas ductility and toughness are controlled to a larger extent by the austenite.[5] The best overall performance with respect to SCC resistance is, therefore, reported for ratios with equal volume fractions of ferrite and austenite.[5,6]

Service temperatures between 523 K and 823 K (250 °C to 550 °C) can limit DSS application due to loss of toughness and ductility arising from microstructure embrittlement.[5,7–10] The highest rate of embrittlement in 22Cr-5Ni DSS was reported to occur at 748 K (475 °C); therefore, this phenomenon is referred to as "748 K (475 °C) embrittlement" or "low-temperature embrittlement" in the literature.[5,9,10] Microstructure embrittlement in this temperature range causes degradation of mechanical properties associated with microstructure decomposition reactions. 748 K (475 °C) embrittlement is usually attributed to phase reactions occurring in the ferrite phase, with the volume fraction of ferrite believed to be a major factor determining component lifetime.[9–11]

Embrittlement is usually ascribed to spinodal decomposition of the ferrite, namely, the formation of Fe-enriched α' phase and Cr-enriched α'' phase, or the formation of Cr-enriched α'' precipitates embedded in a Fe-rich α' matrix after aging in the 523 K to 823 K (250 °C to 550 °C) temperature window.[9,12–16] Ferrite is not stable within the miscibility gap and, therefore, decomposes into two phases. However, additional phases can also form in the ferrite and coexist with the spinodal decomposition products, such as G and R phase, as well as other secondary phases,[7,9–12, 17–27] which also can have significant impact on mechanical properties.

Decomposition and phase reactions in austenite similar to that of ferrite may also occur due to an existing miscibility gap in the Fe-Ni equilibrium phase diagram.[28–32] Therefore, the phenomenon of 748 K (475 °C) embrittlement in DSSs may be associated with a variety of phase transformations occurring in ferrite and in austenite as well. However, ferrite is substantially

CEM ÖRNEK is with the Materials and Performance Centre and School of Materials, The University of Manchester, Sackville Street, Manchester M13 9PL, UK, and also with the Corrosion and Protection Centre, School of Materials, The University of Manchester, and also with the Division of Surface and Corrosion Science, KTH Royal Institute of Technology, 10044 Stockholm, Sweden. Contact emails: ornek@kth.se, cem.oernek@manchester.ac.uk, and cem_oernek@hotmail.de M.G. BURKE is with the Materials and Performance Centre, School of Materials, The University of Manchester. T. HASHIMOTO is with the Corrosion and Protection Centre, School of Materials, The University of Manchester. D.L. ENGELBERG is with Materials and Performance Centre, School of Materials, The University of Manchester, and also with the Corrosion and Protection Centre, School of Materials, The University of Manchester.

Manuscript submitted July 14, 2015.
Article published online January 17, 2017

more prone to phase transformation than austenite due to larger Cr and Mo contents and higher diffusion rates of alloying elements, resulting in faster reaction kinetics in the ferrite.[10,33,34] Thus, the characterization of 748 K (475 °C) embrittlement has mainly focused on phase transformation reactions occurring in the ferrite phase, and therefore, microstructure changes in the austenite have often been disregarded.

The work reported in this article aims to provide an in-depth understanding of microstructure development with correlation to changes in mechanical properties and fracture behavior of 748 K (475 °C)—embrittled 22Cr-5Ni DSS.

II. EXPERIMENTAL

A mill-annealed (as-received) grade 22Cr-5Ni DSS plate with a composition (wt pct) of 22.4Cr, 5.8Ni, 3.2Mo, 1.5Mn, 0.4Si, 0.016C, 0.18N, and Fe (bal.), manufactured by Outokumpu, Sweden, was used for all microstructure investigations in this study. Rectangular coupon specimens were cut from as-received plate and heat treated at 748 K ± 5 K (475 °C ± 5 °C) for 5, 20, 50, and 255 hours, followed by a water quench. The furnace temperature was controlled using a *K*-type thermocouple.

A. *Microstructure Characterization*

The surface of the specimens was prepared by grinding to 4000 grit, followed by fine polishing using 3-, 1-, 0.25-, and 0.1-μm diamond paste, finalized with an OP-S active oxide suspension polishing containing 40-nm colloidal silica particles (pH 9-10). Microstructure characterization and microhardness values were obtained from these surfaces. For high-resolution scanning electron microscopy (SEM) observations, an FEI Magellan high-resolution SEM was used in through-the-lens (TLD) imaging mode using 2 kV and 25 pA. For representation of a macroscopic view of the as-received duplex microstructure, one specimen was prepared for analysis using a Zeiss optical microscope. The specimen was ground and polished to 0.25 μm and chemically etched with Groesbeck reagent (100-mL water, 4-g NaOH, 4-g KMnO4; room temperature), which stains the ferrite.

Thin foil specimens were prepared by electropolishing 80- to 100-μm-thick and 3-mm-diameter disc samples in the Tenupol-5 twin jet polisher (Struers, Denmark) with a Jubalo closed-cycle refrigeration system. The samples were electropolished at 20 kV in an electrolyte of a mixture of 20 vol pct perchloric acid and 80 vol pct methanol at a temperature of 233 K (–40 °C). All specimens were subsequently examined in an FEI Tecnai F20 200 kV analytical transmission electron microscope (TEM), equipped with an Oxford Instruments Xmax80-TLE SDD energy-dispersive X-ray detector operated with an AZtec analysis system, and an FEI Talos field-emission gun analytical TEM equipped with Super X (4 SDDs).

B. *Hardness Testing*

Macrohardness measurements were carried out on a Vickers macrohardness device (Georg Reicherter Briviskop 187.5) with a load of 30 kg (HV30). For each sample, 10 hardness indentations were made and the arithmetical mean with standard deviation calculated. All samples had 600-grit SiC paper ground surface. Macrohardness testing was augmented by microhardness measurements to obtain information about the behavior of individual microstructure constituents with 748 K (475 °C) embrittlement treatment.

Microhardness measurements were conducted with the Struers Duramin microhardness tester (Ballerup, Denmark) with a Vickers indenter and a test load of 0.098 N (HV0.01). The surface finish of all tested samples was 0.25-μm polish. A total of 50 hardness measurements were obtained from each specimen: 25 measurements in the austenite phase and 25 measurements in the ferrite one. Ferrite and austenite could be easily discerned in the backscatter electron imaging mode in the SEM FEI Quanta 650, and each indent size was measured and the arithmetic mean of all microhardness results calculated.

C. *Tensile Testing*

Tensile tests were performed to obtain mechanical properties of flat tensile specimens, with parameters determined as 0.2 pct offset yield stress, $R_{p0.2}$, and ultimate yield stress, R_m. A mill-annealed sheet 22Cr-5Ni DSS was used for all tensile tests with a composition of 22.44Cr, 5.75Ni, 3.32Mo, 1.41Mn, 0.42Si, 0.015C, 0.155N, 0.006Nb, 0.21Cu, 0.12Co, and Fe (bal.). Tensile tests were performed on an Instron 5569 tensile testing machine with an extensometer from MTS. The strain rate was 2 mm/min. Tensile specimens, with 50-mm gage length, 10-mm gage width, and a total length of 80 mm, were machined from 2-mm-thick grade 22Cr-5Ni DSS sheet. The fracture surfaces of the as-received and 20-, 50-, and 255-hour aged conditions were analyzed using the FEI Quanta 650 SEM. The fracture area and degree of embrittlement were quantified using the ImageJ image processing programme (https://imagej.nih.gov/ij/).

III. RESULTS AND DISCUSSION

A. *Microstructure Characterization*

The microstructure of the as-received condition in the rolling direction (RD) is shown in Figures 1 and 2 for the plate and sheet materials, respectively. Ferrite (δ-bcc) and austenite (γ-fcc) phases with typical ferrite/austenite grain boundaries can be seen, whereas the ferrite/ferrite and austenite/austenite boundaries are not visible. The phase ratios of austenite to ferrite (as-received) were previously reported as 56:44 and 54:46 for the plate and sheet materials, respectively.[35,36] The grain size of the plate material in the RD of ferrite was 10.4 ± 3.2 μm, while the grain size of

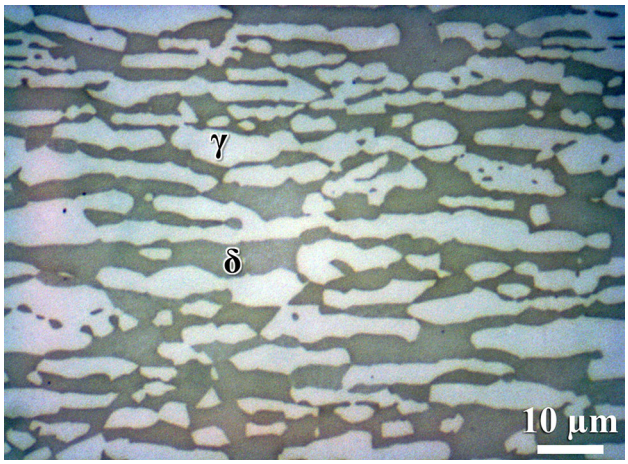

Fig. 1—Optical micrograph showing the as-received microstructure of the plate material. Groesbeck etching with magnification 1000 times.

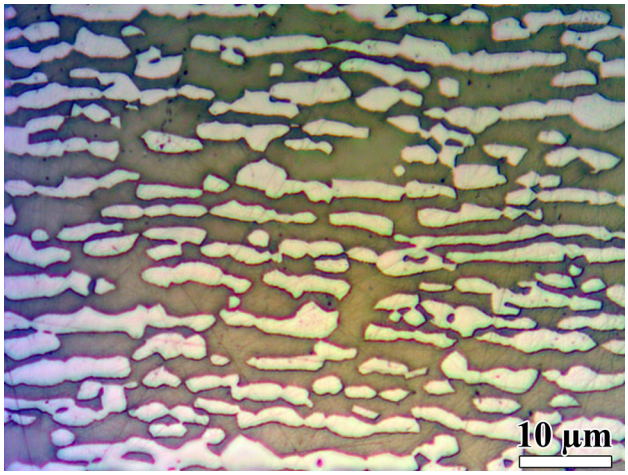

Fig. 2—Optical micrograph showing the as-received microstructure of the sheet material. KOH etching with magnification 1000 times showing ferrite (dark) and austenite (bright).

austenite was 10.7 ± 3.6 μm. The average aspect ratio (horizontal-to-vertical mean length) was 2.5 for ferrite and 1.9 for austenite. The grain size of the sheet material in the RD of ferrite was 4.2 ± 2.3 μm, while the grain size of austenite was 2.2 ± 1.4 μm. The sheet material was expected to behave in a similar manner to the plate.

More detailed microstructure information of the austenite and ferrite was obtained through TEM analysis (Figure 3). In the as-received condition, austenite grains were characterized by the presence of stacking faults and some dislocations, consistent with a recrystallized microstructure. The ferrite contained dislocation loops, consistent with a deformed or recovered microstructure. This indicates the presence of residual strain from the thermomechanical process history of the as-received material. No crystallographic phases other than the austenite and ferrite were detected in the as-received material.

The sample aged for 5 hours had a mottled contrast in the ferrite, most likely associated with spinodal decomposition products, as shown in the high-angle annular dark-field (HAADF) image in Figure 4. The mottled contrast is related to compositional differences between Fe-rich α' and Cr-enriched α''. This is in line with the work of Weng *et al.*[16] who reported spinodal structures of 1 to 2 nm in the ferrite of 22Cr-5Ni DSS after 2 hours of aging at 748 K (475 °C). No other phases were observed.

The microstructure of the specimen aged for 20 hours was characterized by the presence of dislocation structures consisting of numerous dislocation loops in the ferrite with dislocation forests on ferritic subgrain boundaries, all indicating high dislocation activity. These can be seen in the bright-field TEM images in Figure 5(a) and (b). These loops were still present after the aging process. Small discrete realms of strain contrast, possibly associated with precipitation incubates, were observed in the ferrite, which can be seen in Figure 5(b). The mottled contrast in the ferrite associated with spinodal decomposition products became more apparent in comparison to the specimen aged for 5 hours. This is an indication of enhancement of the amplitude of spinodal decomposition (*i.e.*, distance of Cr-enriched α'' and Fe-rich α' regions) in ferrite, which can be seen in Figure 5(c). This observation is in good agreement with the work of Weng *et al.*[16] who reported spinodal decomposition of 2- to 4-nm size after 16 hours of aging at 748 K (475 °C) of a 22Cr-5Ni DSS. In austenite, numerous stacking faults and a deformation structure were observed, as shown in Figure 5(d).

The microstructure after 50 hours of aging contained numerous *R*-phase precipitates, which could already be seen in the SEM, as shown in Figure 6. The sizes of these precipitates varied between 20 and 50 nm and were located within ferrite grains only. Further secondary phases seemed to coexist with the *R* phase along interphase boundaries.

Significant microstructure changes were evident after aging at 748 K (475 °C) for 255 hours. The microstructure containing decomposed ferrite with numerous precipitates is shown in Figure 7. The majority of these precipitates could be ascribed to *R* phase. *R*-phase precipitates showed disc or lenticular shape in sizes between 50 and 400 nm and nucleated at inter- and intragranular sites in ferrite grain interiors and at ferrite grain boundaries, as shown in Figure 8. Some ferrite regions were enriched in *R* precipitates, where high-angle grain boundaries (HAGBs) and low-angle grain boundaries (LAGBs) seemed to function as preferential nucleation sites. *R*-phase precipitates arrayed along slip planes and LAGBs can be seen in Figures 7 and 8. The formation of *R* was heterogeneous, and discrete precipitation occurred in certain ferrite regions. A precipitation density of 13 particles per square micrometer, on average, in the ferrite was calculated using Image J software from TEM images. Since precipitation was heterogeneous, the particle density can be significantly higher in regions containing more precipitates. No phase transformation products could be observed in the austenite. These observations are in good agreement with Nilsson and Liu,[19] Redjaimia *et al.*,[12,37] and Karlsson *et al.*[21] who observed *R*-phase precipitates at 823 K (550 °C), 873 K (600 °C), and 948 K (675 °C),

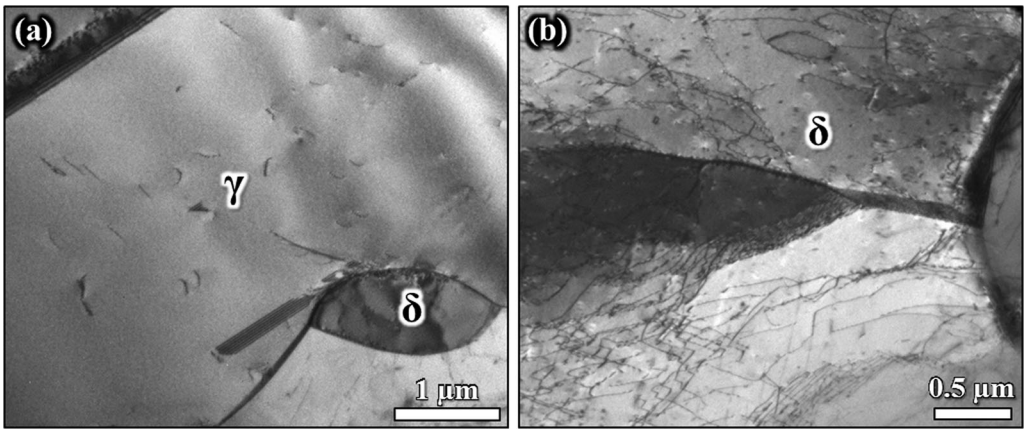

Fig. 3—As-received microstructure using TEM bright-field imaging showing (*a*) a smooth structure and stacking faults in austenite and (*b*) a pile of dislocations and loops in ferrite.

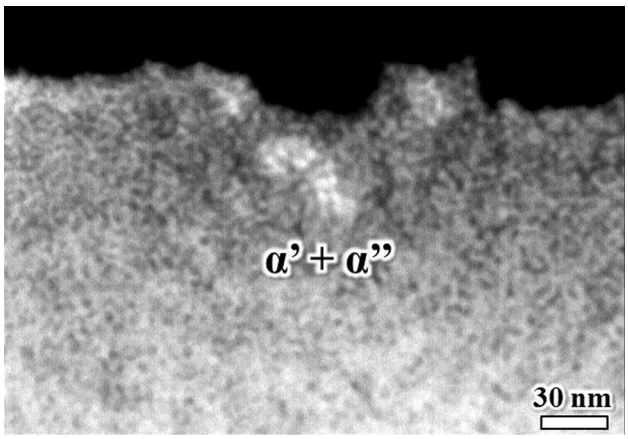

Fig. 4—TEM image of the microstructure aged at 748 K (475 °C) for 5 h showing a mottled contrast in ferrite associated with spinodal decomposition consisting of Fe-rich α′ and Cr-enriched α″ (HAADF image).

respectively. They also found Mo- and Si-depleted zones at and adjacent to *R* precipitates.

Higher magnification TEM images of a region containing *R*-phase precipitates revealed stronger diffraction contrast than the surrounding ferrite matrix, as shown in the BF- and DF-TEM images in Figure 9. *R* precipitates seemed to be heavily faulted and had lenticular morphologies, in good agreement with previous studies.[12,19,21, 37] Spinodal decomposition in ferrite became more apparent in SEM analyses, as shown in Figure 10. This mottled structure is the intertwined, three-dimensionally interconnected Cr-rich α″ and Fe-rich α′ phase, which was confirmed by TEM diffraction analysis. The bright appearing features are Cr-Mo–enriched α″. They protrude out of the Fe-enriched α′ matrix. The spinodal arm width of α″ was determined to be 15 to 30 nm, and the ferrite seemed to have decomposed entirely.

B. *Mechanical Behavior*

The hardness test results are summarized in Figure 11. A slight increase in hardness with aging up to 50 hours was observed, with a significant rise in macrohardness in the specimen aged for 255 hours, clearly indicating the effect of 748 K (475 °C) embrittlement. The microhardness of the ferrite followed a similar trend, except for the 20-hour aged specimen, with maximum hardness observed after 255 hours. Phase transformation reactions occurring in ferrite resulted in a hardness increase. The hardness of austenite remained constant between a minimum of 263 HV0.01 and a maximum of 290 HV0.01. This indicates that no significant microstructure change occurred that could have influenced the hardness values in austenite. The hardness increase of the ferrite is due to the mismatch of the elastic moduli and lattice parameters between the components of the decomposed ferrite requiring more stress for dislocation mobility.

Bulk hardness delivered more global information, whereas microhardness gave local information of each microstructure constituent. The bulk hardness is a convolution of the hardness of both ferrite and austenite phases, whereas the microhardness data for each phase gives local information. Microhardness measurement, however, gives local hardness of the microstructure and is a convolution of grain orientation and precipitation heterogeneity, which causes different hardness values within the ferrite. It is evident that the scattering for austenite is less than that for ferrite, supporting this statement. It has become evident that the ferrite is affected by aging at 748 K (475 °C), whereas the austenite seemed to not show a significant change in local hardness. Precipitates mainly caused a hardness increase in the ferrite, which was more apparent after 255 hours of aging.

All tensile test results for the as-received and 20-, 50-, and 255-hour aged specimens are shown in Figure 12. The elongation to failure (*A*) halved after 20 hours aging from 50 ± 5 to 28 ± 6 pct, showing clear signs of embrittlement. The largest embrittlement was observed in the 255-hour aged specimen, with only 12 ± 4 pct of elongation to failure. The yield stress, $R_{p0.2}$, increased to 735 ± 35 MPa after 255 hours of aging. The ultimate tensile strength rose from 830 ± 20 to 1030 ± 20 MPa after 255 hours of aging. Precipitates and spinodal decomposition can impede dislocation movement and,

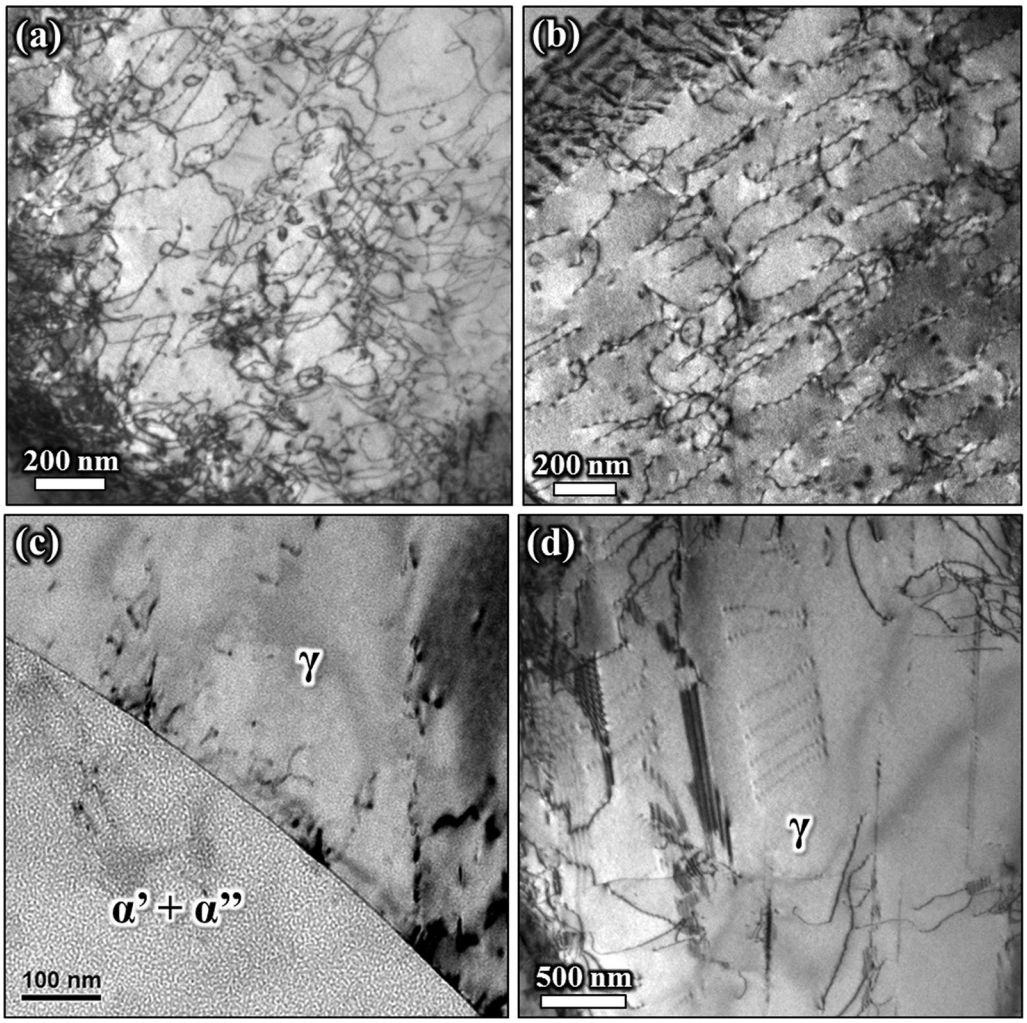

Fig. 5—TEM bright-field analysis of the microstructure aged at 748 K (475 °C) for 20 h showing (*a*) and (*b*) a pile of dislocations and loops in the ferrite, with (*c*) showing the mottled contrast in ferrite associated with spinodal decomposition, and (*d*) stacking faults and a minor deformation structure in austenite.

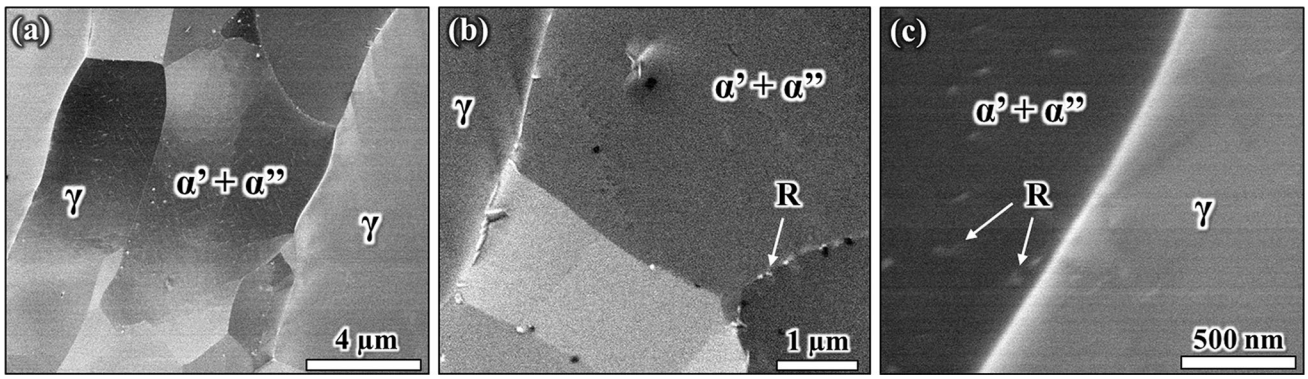

Fig. 6—SEM analysis of the microstructure aged at 748 K (475 °C) for 50 h showing (*a*) an overview with (*b*) and (*c*) showing secondary phases located in ferrite and on interphase boundaries.

hence, the onset of plasticity. This leads to an increase in yield strength, which is associated with a decrease in toughness. Aging at 748 K (475 °C) caused microstructure strengthening at the expense of increasing embrittlement.

The observed embrittlement was also manifested by a large drop in uniform and total elongation, evident in the stress-strain behavior of all aged samples. The 255-hour aged sample, for example, showed immediate failure upon reaching ultimate tensile stress, as shown in

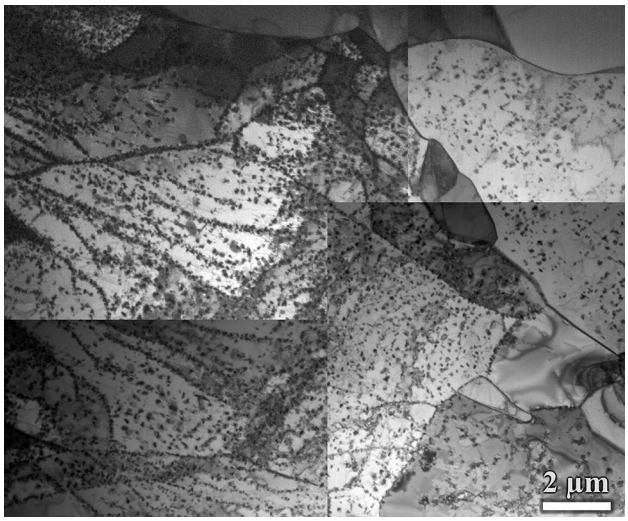

Fig. 7—TEM bright-field montage of the microstructure aged at 748 K (475 °C) for 255 h over a large ferrite area containing numerous precipitates.

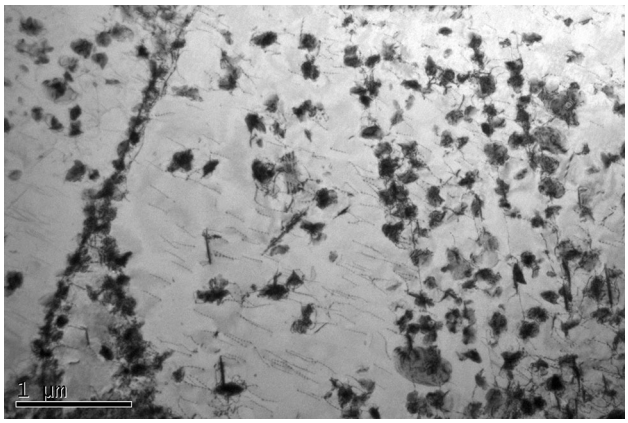

Fig. 8—TEM bright-field image of the microstructure aged at 748 K (475 °C) for 255 h with *R*-phase precipitates in the ferrite.

Figure 13. Both uniform and total elongations are a measure of material ductility and formability. Both uniform and total elongations were decreased sharply by aging time, with short-term aging showing a much steeper drop in ductility. This is evidence that short-term aging can already significantly deteriorate material ductility. Spinodal decomposition seems to have a larger impact on ductility than on hardness, since the hardness of both ferrite and austenite was not affected during short-term treatments at 748 K (475 °C) in DSS.

Spinodal decomposition and precipitation in the ferrite phases seems to be primarily responsible for most mechanical property degradation. This is because ferrite is the matrix phase in the duplex microstructure and, hence, the main load carrying element.

C. *Fracture Surface Analysis*

The fracture surfaces of all tensile specimens are shown in Figure 14. The cross-sectional area of the fracture surface increased from 5.2 to 9.1 mm^2 after 255 hours of aging, as summarized in Figure 13. This is related to a reduced ductility, resulting in earlier fracture with less necking. The largest necking was observed on the as-received condition, which gradually decreased with aging time, confirming embrittlement. There is a large loss of ductility associated with heat treatment at 748 K (475 °C), as shown in Figure 12.

The fracture surface of the as-received microstructure is given in Figure 15. Most necking was observed in the as-received condition, indicating the highest ductility and toughness among all heat-treated specimens. Microvoid coalescence was the main fracture mode, as visible from prominent cup-and-cone-shaped structures, indicating ductile fracture. These dimples were observed all over the fractured surface, indicating ductile rupture behavior of both ferrite and austenite grains. Most dimples were equiaxed, typical for strain acting normal to the fracture surface. Elongated dimples were also observed, particularly in the vicinity of the main crack (Figure 15(e) and (f)) and in regions showing signs of cleavage fracture (Figure 15(c) and (d)). Elongated dimples typically indicate shear deformation, clearly evidencing ductile fracture behavior. These observations are in good agreement with Pettersson *et al.*[38] and de Lacerda *et al.*[39] who also reported ductile fracture surface for DSS in the as-received condition (solution annealed). Easy slip activity from ferrite and austenite, and *vice versa*, is reported for as-received duplex microstructure.[11] Austenite accommodates most plastic strain due to its closely packed slip systems. However, the austenite is not continuous, so the ferrite can limit slip activity, which requires slip interchange between austenite and ferrite. Plastic deformation of ferrite usually results in deformation twins, which lead to high stored energy in the microstructure and to cleavage rupture.[16,38,40]

The fracture surface of the 20-hour aged specimen is shown in Figure 16. Ductile fracture by microvoid coalescence governed the fracture surface, with some regions, indicating quasi-cleavage. Most microvoids were nonequiaxed, and numerous cavities were seen decorating the fracture surface, indicating loss of constraint and delamination rupture along interphase boundaries. Loss of toughness and ductility associated with 748 K (475 °C) embrittlement was reported due to the inability of the ferrite to form deformation twins.[38,41] Spinodal decomposition in the ferrite retards slip activity requiring more energy for slip interchange between ferrite and austenite. Spinodal decomposition is reported to be associated with higher elastic strain energy due to different atomic sizes between iron and chromium atoms.[11] Hence, the reduced ability to plastically deform ferrite resulted in austenite being constrained, leading to less ductile fracture. Decoherence between ferrite and austenite grains led then to delamination and cleavage fracture.

The fracture surface of the 50-hour aged condition can be seen in Figure 17. More extensive cracking was observed with significantly less necking and less dimples, all indicating embrittlement. Cleavage fracture areas were observed, which indicated strain heterogeneity in the microstructure. *R*-phase precipitates and further

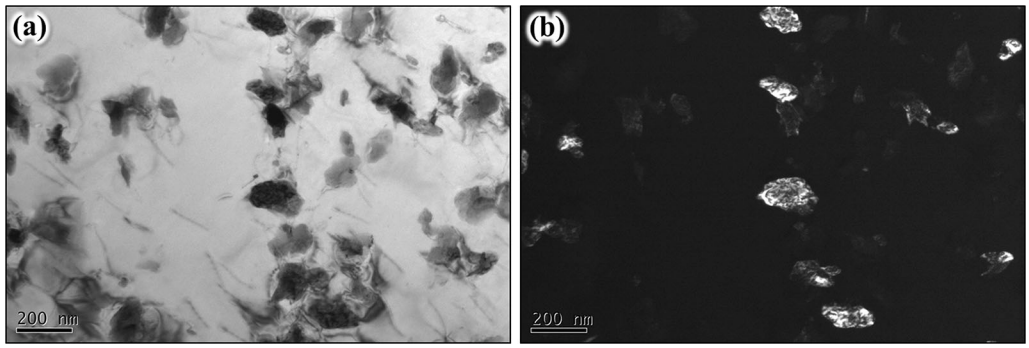

Fig. 9—TEM analysis of the microstructure aged at 748 K (475 °C) for 255 h showing *R* precipitates at higher resolution with (*a*) bright-field image and (*b*) the corresponding dark-field image.

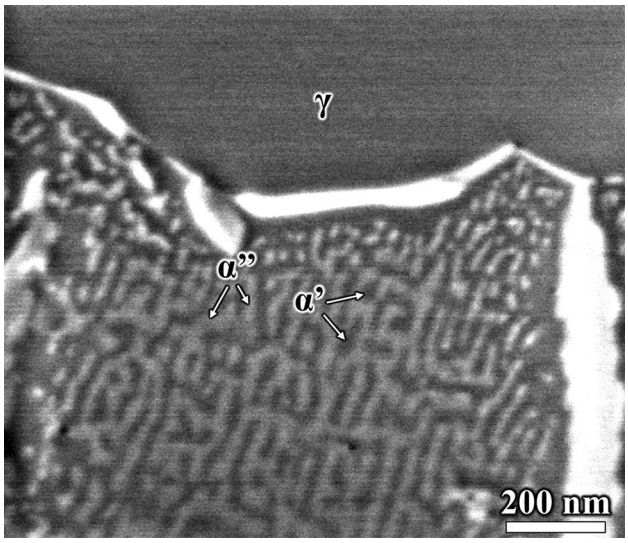

Fig. 10—Microstructure development after aging at 748 K (475 °C) for 255 h showing spinodally decomposed ferrite with no phase transformation products in austenite (SEM-TLD image).

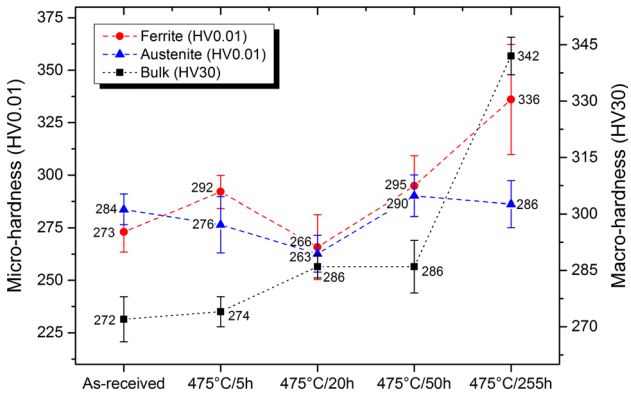

Fig. 11—Macrohardness (bulk) and microhardness development with 748 K (475 °C) exposure for up to 255 h.

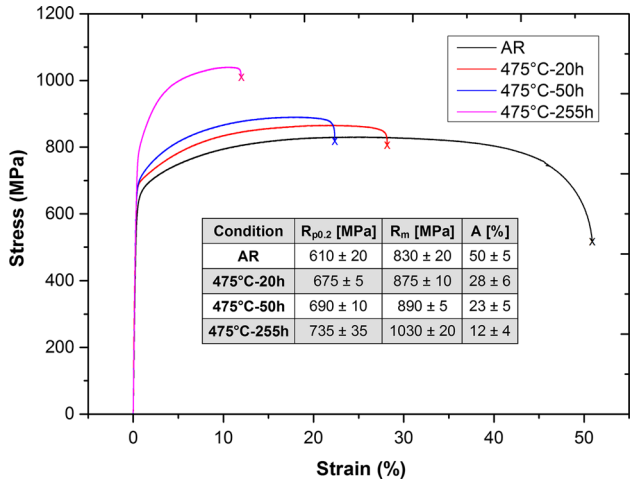

Fig. 12—Stress-strain behavior as a function of aging time at 748 K (475 °C) (AR: as received, R_m: ultimate tensile strength, A: elongation to failure, and $R_{p0.2}$: yield strength).

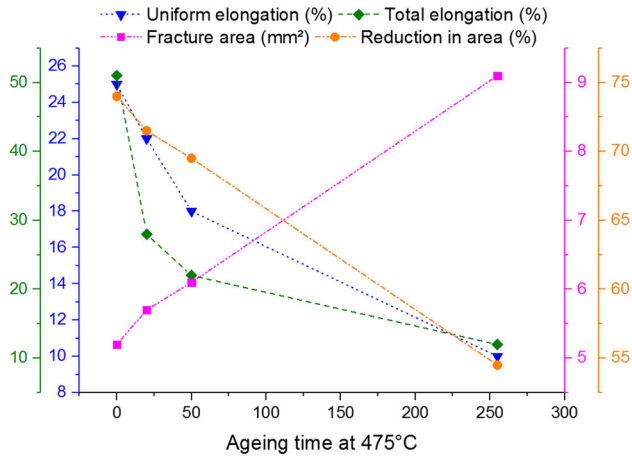

Fig. 13—Evaluation of tensile test and fracture surface results.

secondary phases in the ferrite most likely led to enhanced slip retardation affecting macroscopic fracture appearance. Hence, slip incompatibility at the interphase boundaries may have resulted in nonuniform distribution of surface damage. Slip bands were seen in certain elongated dimpled regions of austenite grains, as shown in Figure 17(d), most likely indicating slip incompatibility at interphase boundaries, resulting in

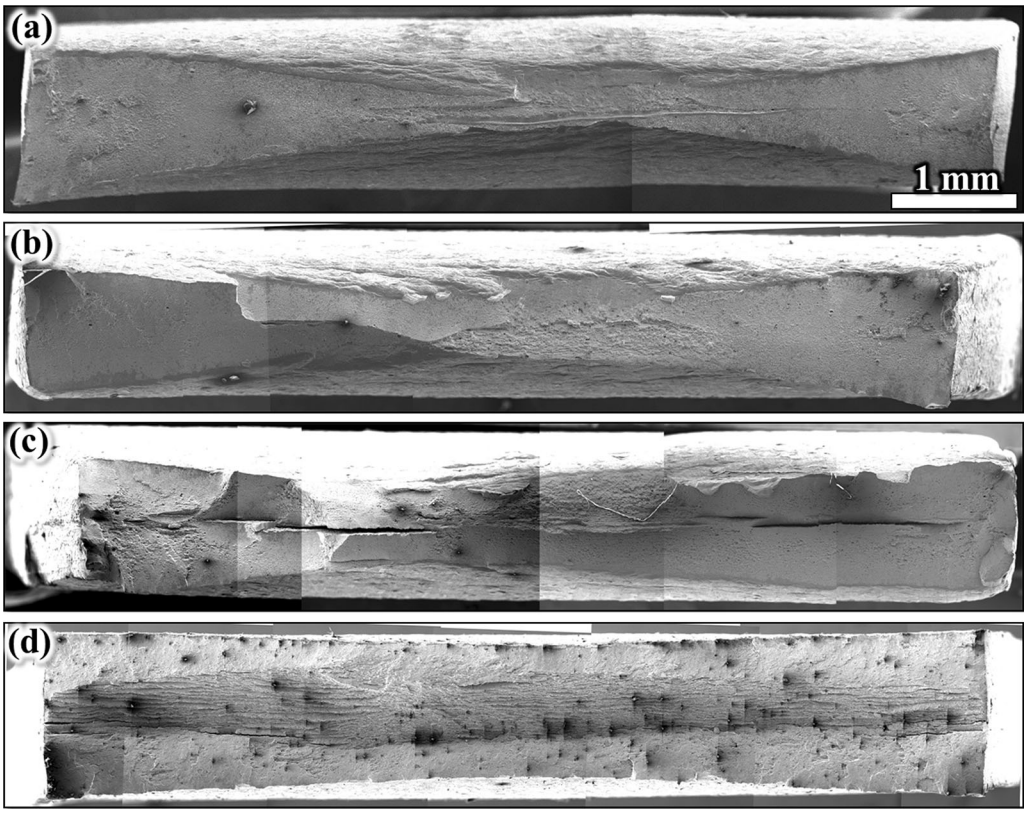

Fig. 14—Overview of the fracture surface of (*a*) as-received, (*b*) 20-h aged, (*c*) 50-h aged, and (*d*) 255-h aged tensile specimens (SE-SEM images).

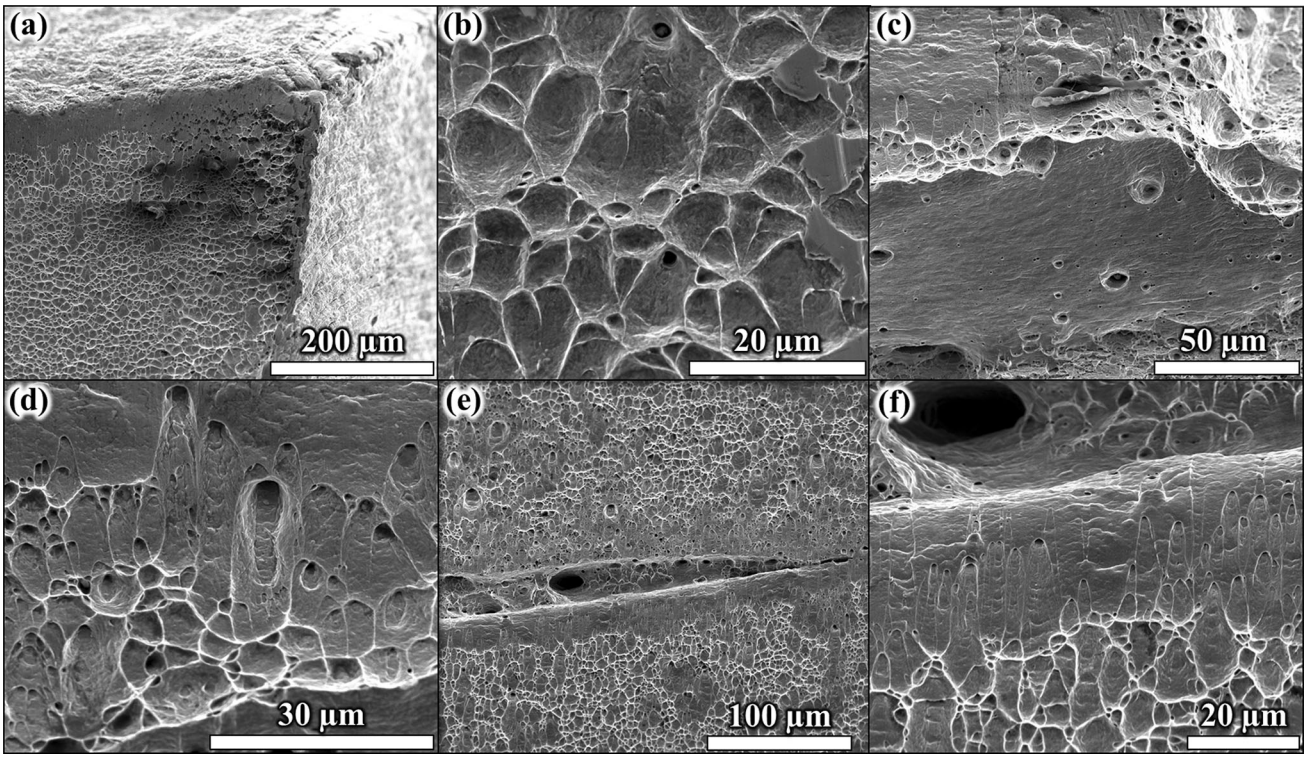

Fig. 15—Fracture surface of the as-received tensile specimen: (*a*) necking occurred with (*b*) cup-and-cone-shaped features (microvoid coalescence) in ferrite and austenite, (*c*) some smooth shear rupture with multiple spherical dimples, (*d*) cup-and-cone-shaped features and spherical dimples in ferrite and austenite, (*e*) normal crack in the center, and (*f*) elongated dimples indicating shear deformation.

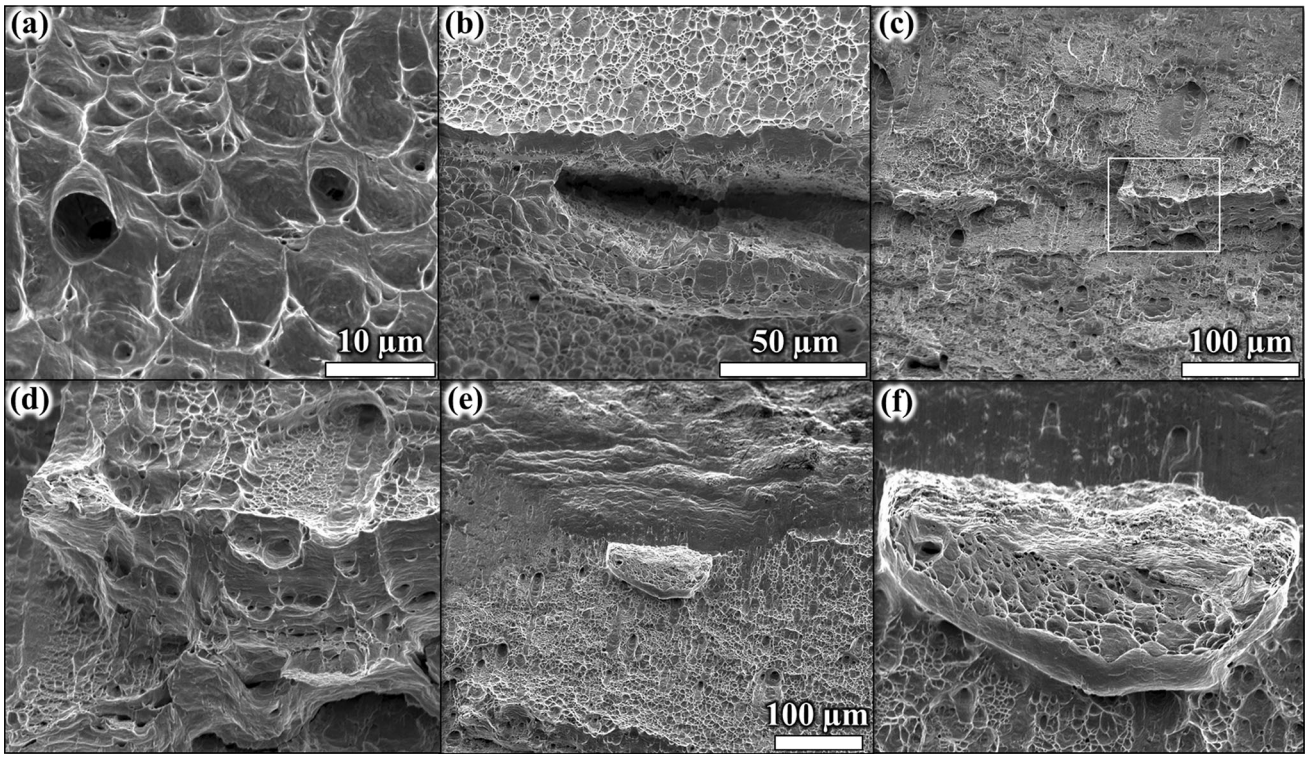

Fig. 16—Fracture surface of the tensile specimen aged at 748 K (475 °C) for 20 h: (*a*) showing microvoid coalescence, (*b*) region with dimple rupture, (*c*) necking with dimple rupture, (*d*) higher magnified view of highlighted region in (c), necked region with dimple rupture, and elongated dimples, (*e*) region showing transition from necking to microvoid coalescence with elongated dimples, and (*f*) higher magnified view of the outstanding fracture part shown in (e).

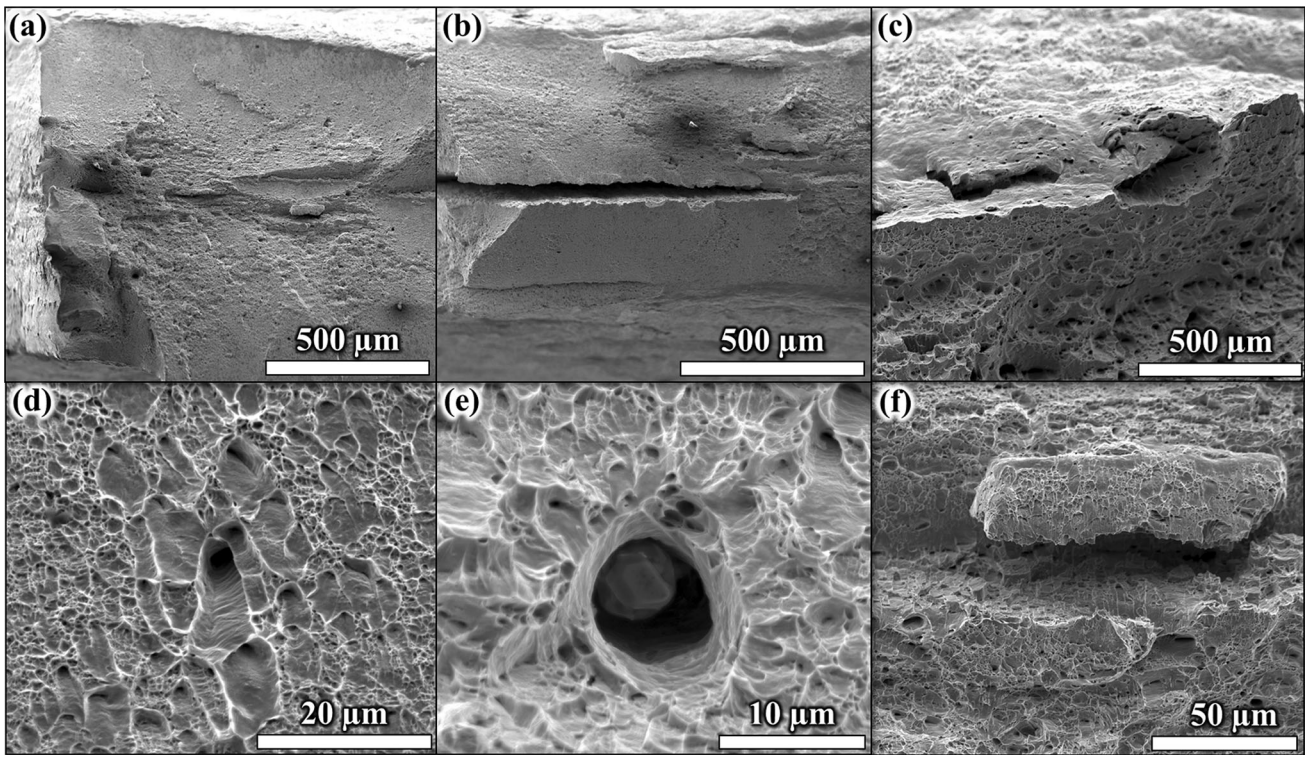

Fig. 17—Fracture surface of the tensile specimen preaged at 748 K (475 °C) for 50 h: (*a*) showing brittle fracture, (*b*) large crack in the center of the cross section, (*c*) necking, (*d*) and (*e*) microvoid coalescence and decohesive rupture, and (*f*) elongated microvoid coalescence and brittle fracture.

easier delamination rupture along ferrite-austenite grain boundaries. Large cavities (Figure 17(e)) and heterogeneous fractured regions (Figure 17(f)) were observed, indicating loss of strain homogeneity and local brittleness. Such sites were most likely associated with high strain fields, in which austenite and ferrite slip systems had low Schmid factors.

The most severe fracture was seen on the specimen aged for 255 hours, as shown in Figure 18. Extensive cracking was noticeable with little necking, indicating the highest 748 K (475 °C) embrittlement among all heat treatment conditions. Long and wide cracks were seen with fibrous appearance, defined as delamination fracture, indicating preferential rupture along interphase boundaries. Similar observations were reported by Pettersson *et al.*[38] and Pilhagen *et al.*[42] who investigated the effect of aging in the 748 K (475 °C) temperature window on the fracture behavior of DSS. They observed delamination cracking associated with enhanced slip incompatibility between ferrite and austenite in combination with cleavage fracture. However, the fracture mechanism was not explained. In our case, ferrite grains containing numerous slip bands are shown in Figure 18(c) and (d). Such features were seen on ferrite grains neighboring austenite grains and along the microstructure processing direction (RD) only. Cracks with wide crack openings were seen along interphase boundaries showing enhanced phase mismatch, as shown in Figure 18(e). In certain austenite regions, transgranular cleavage tongues were present (Figure 18(e)), indicating the loss of strain homogeneity and enhanced local embrittlement. This showed loss of ductility of the austenite, supporting the overall embrittlement phenomenon, which is in line with the work of Pettersson *et al.*[38] who observed similar cleavage tongues on 748 K (475 °C)—embrittled fractured 2507 super DSS. Cleavage tongues are signs of a decrease of the overall fracture energy.[38]

Marrow and Harris[43] studied the fracture behavior of 748 K (475 °C)–embrittled Zeron 100 super DSS and concluded that the brittle fracture of ferrite is twin nucleated. Thus, twinning is necessary for ferrite cleavage and crack initiation is controlled by the critical shear stress, which decreases with aging. However, when the critical shear stress is higher than the shear stress for twin or slip band nucleation and yield, fracture occurs with no or minor plastic deformation. There is strain and stress partitioning among both crystallographic phases in duplex steels.[44] Stress partitioning to the ferrite occurs by plastic deformation of the softer austenite, which in turn increases the stress in the ferrite.[43,44] The internal friction of ferrite is affected by the 748 K (475 °C) embrittlement heat treatment, whereas the friction stress of austenite is believed to be nonaffected by age hardening. Therefore, long-term aged microstructures were more affected due to the

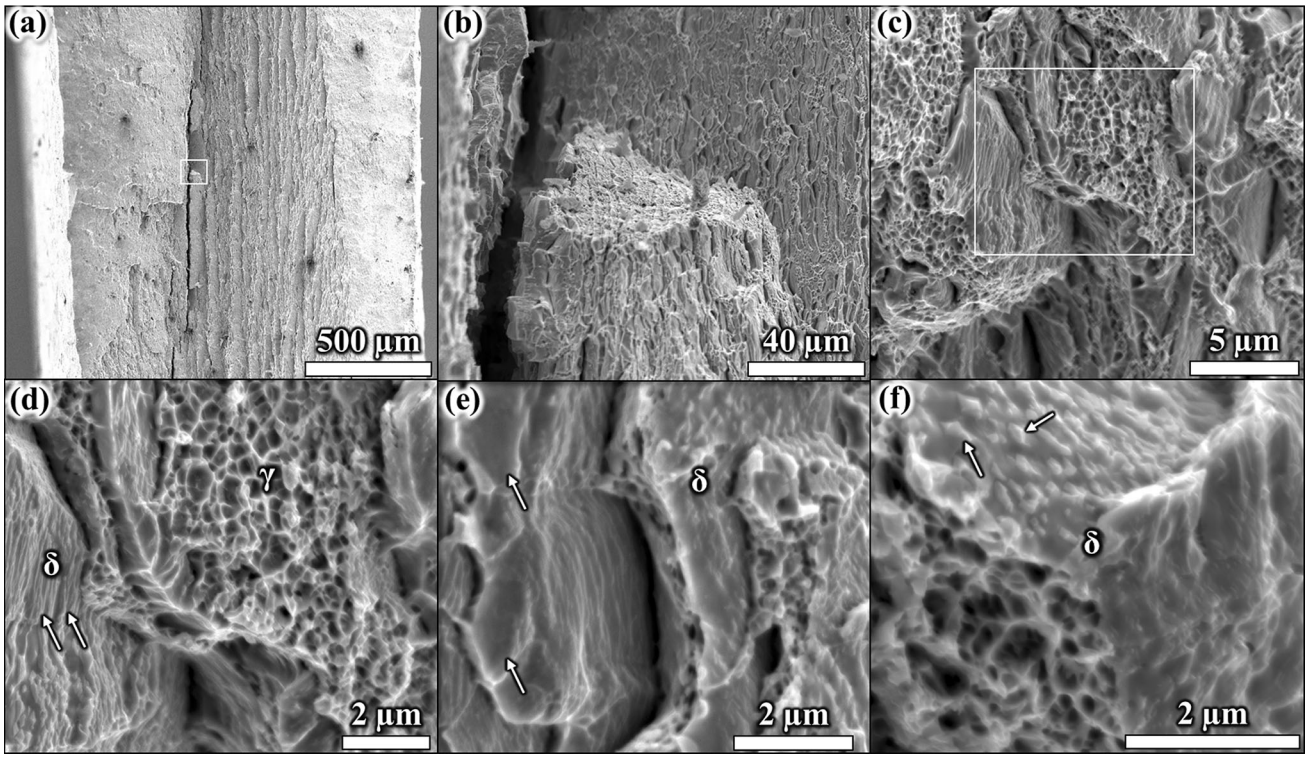

Fig. 18—Fracture surface of the tensile specimen preaged at 748 K (475 °C) for 255 h: (*a*) showing delamination rupture (vertical fracture features); (*b*) higher magnified view of the highlighted region in (*a*), showing decoherence between ferrite and austenite grains; (*c*) microvoid coalescence in austenite grains and transgranular cleavage in ferrite grains; (*d*) higher magnified view of the highlighted region in (*c*); (*e*) showing crack following an interphase boundary, indicating decoherence between ferrite and austenite with transgranular cleavage tongues on austenite and microvoid coalescence of ferrite; and (*f*) higher magnified view of (*e*) showing precipitates standing out from ferrite grains most likely associated with the microvoids.

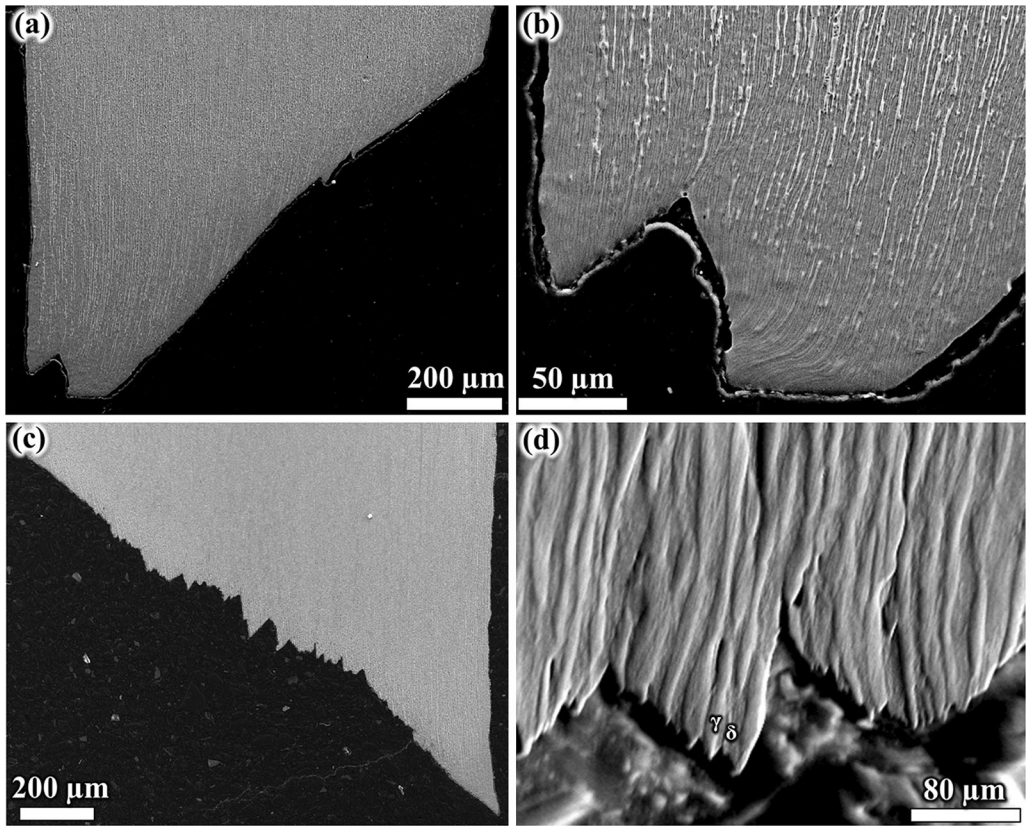

Fig. 19—Cross-sectional fracture surface of (*a*) and (*b*) the as-received tensile specimen and (*c*) and (*d*) the tensile specimen preaged at 748 K (475 °C) for 255 h.

increased differences of the flow stresses of both ferrite and austenite. Marrow and Harris[43] argued that 748 K (475 °C) embrittlement is not accompanied by the precipitation of a brittle phase and neglected secondary brittle phase formation in the austenite. There is a high fraction and density of precipitates in the ferrite (Figure 7). The lattice parameters of the *R* phase are approximately seven times larger than those of the ferrite,[37] and the *R* phase is considered as the harder phase, so that dislocation cutting through the particles is not possible, for larger particles at least. Dislocation bowing around these phases would be the hardening mechanism in the ferrite. Therefore, the fracture mechanism of long-term embrittlement DSS, containing high fractions of precipitates, would be precipitation hardening controlled.

Fine-scale dimples in ferrite grains were also seen, which indicated rupture. These dimples were associated with the large number of precipitates in the ferrite causing microvoid coalescence and may have resulted in inter- and transgranular cleavage. There is a clear change of fracture mechanism noticeably associated with 748 K (475 °C) embrittlement. Austenite, in contrast, fractured in a ductile manner and seemed to accommodate most plastic deformation. Hence, ferrite alone can be made responsible for the 748 K (475 °C) embrittlement of 2205 DSS.

Analysis of the cross-sectional fracture surface of the as-received specimen showed extensive necking, with large local plastic deformation at the ruptured fracture surface regions. The fracture surface had a smooth appearance with both ferrite and austenite showing extensive deformation at the rupture area, shown in Figure 19(a) and (b). Both phases accommodated large plastic strains prior to rupture, indicating that ample cross-slip of dislocations among both phases was possible. Despite the extensive strain hardening at the necked area, a broad zone of bent and elongated austenite and ferrite grains was observed on the fracture surface, indicating ductility. In contrast, the fracture surface of the specimen aged for 255 hours had a zigzag pattern with very little necking. Almost the entire population of ferrite grains fractured at an angle of ~45 deg, with respect to the tensile direction, indicating brittle failure. This also indicated that almost no yielding occurred and that fracture occurred after little or no yielding. The ferrite seemed not to show the classic fracture shape, in which necking followed by a fibrous fracture occurs, whereas the austenite showed some necking, indicating ductile behavior. However, there was also a minor loss of ductility noticed in the austenite associated with 748 K (475 °C) embrittlement. The fracture of the ferrite was transgranular, showing a similar typical appearance to low-temperature cleavage

rupture of nonembrittled steels. Thus, the ferrite was the phase mainly responsible for the brittle fracture.

The fracture area increased and the reduction in area decreased with increasing aging time. There seemed to be a linear relationship between fracture area and aging time at 748 K (475 °C) and likewise for the reduction in area (Figure 13). The reduction in area on the as-received material was 74 pct, whereas after 255 hours of aging, a final reduction in area of 54.5 pct was measured. The effect of aging on the reduction in area was less than on uniform and total elongation, which means that material deformation in cross-sectional areas was more pronounced than along the tensile direction.

Tensile properties are seemingly enhanced, and most plastic deformation was observed perpendicular to the loading direction, causing large contraction and perhaps even local compression of the ductile austenite grains. Forged DSSs typically have, due to their processing history, nonequiaxed grain structure with elongated or flattened grain shapes. Mechanical properties, accordingly, are dependent upon the microstructure processing orientation. Decomposition products of ferrite reduced the ability for uniaxial tensile deformation; therefore, plastic deformation concentrated on the austenite, acting perpendicular to the loading direction.

In summary, the fracture behavior of 748 K (475 °C)–embrittled 22Cr-5Ni DSS is controlled by precipitation hardening occurring in the ferrite phase, not only by spinodal decomposition. This is clearly noticeable from the hardness trend and fracture behavior, as shown previously. The phase mismatch between ferrite and austenite increases with age hardening; hence, their flow stress increases, causing delamination fracture.

IV. CONCLUSIONS

Aging treatments of 22Cr-5Ni DSS at 748 K (475 °C) for 5, 20, 50, and 255 hours resulted in microstructure changes in the ferrite phase, which directly affected the mechanical properties and fracture behavior.

1. Hardness measurements showed substantial changes after 255 hours of aging only, with the ferrite responsible for the increase in hardness.
2. Higher yield strengths and ultimate tensile strengths were observed associated with a loss of ductility with increasing aging time at 748 K (475 °C).
3. Spinodal decomposition, consisting of Fe-enriched α' and Cr-enriched α'', was observed in ferrite with increasing amplitude as a function of aging time.
4. Numerous *R*-phase precipitates with disc or lenticular shape and sizes between 50 and 400 nm could be detected after 50 and 255 hours of aging. The precipitates seemed to be mainly responsible for the increase of hardness and strength and the loss of tensile toughness.
5. Fracture surface analyses revealed a transition from ductile dimple fracture of the as-received condition to macroscopic delamination fracture associated with slip incompatibility and decoherence between ferrite and austenite after 255 hours of aging.
6. The ferrite became brittle, mainly due to the presence of numerous precipitates, whereas the austenite was ductile and accommodated most plastic strain.

ACKNOWLEDGMENTS

The authors acknowledge EPSRC (Grant No. EP/I036397/1) and NDA (Grant No. NPO004411A-EPS02) for financial support. The authors are grateful for the kind provision of Grade 22Cr-5Ni Duplex Stainless Steels by Rolled Alloys. Further thanks are extended to Gary Harrison, University of Manchester, for his support during XRD measurements. The authors are also grateful to Dr. Philip Platt, University of Manchester, for valuable feedback.

OPEN ACCESS

REFERENCES

1. J. Charles: *Steel Res. Int*., 2008, vol. 79, pp. 455–65.
2. J. Charles and S. Bernhardsson: *Duplex Stainless Steels '91*, Beaune, Les editions de physique, 1991, vol. 1, pp. 3–48.
3. J. Charles and S. Bernhardsson: *Duplex Stainless Steels '91*, Beaune, Les editions de physique, 1991, vol. 2, pp. 711–18.
4. S. Li, Y. Wang, and X. Wang: *Mater. Sci. Eng. A*, 2015, vol. 625, pp. 186–93.
5. R.A. Lula: *Duplex Stainless Steels*, ASM, Mars, PA, pp. 693–756.
6. R. Pettersson and E. Johansson: *Duplex World 2010*, Duplex Stainless Steel World, Beaunne, 2010.
7. F. Wischnowski: Ph.D. Thesis, Technical University of Bochum, Bochum, Germany, 1995, p. 264.
8. O.K. Chopra and H.M. Chung: Report No. CONF-870839-8, Argonne National Laboratory Materials and Components Technology Division, Argonne, IL, June 1987.
9. K.H. Lo, C.H. Shek, and J.K.L. Lai: *Mater. Sci. Eng. R*, 2009, vol. 65, pp. 39–104.
10. H.-J. Eckstein: *Korrosionsbeständige Stähle*, Deutscher Verlag für Grundstoffindustrie GmbH, Leipzig, 1990, pp. 1–264.
11. J.K. Sahu, U. Krupp, R.N. Ghosh, and H.J. Christ: *Mater. Sci. Eng. A*, 2009, vol. 508, pp. 1–14.
12. A. Redjaïmia, J.P. Morniroli, P. Donnadieu, and G. Metauer: *J. Mater. Sci*., 2002, vol. 37, pp. 4079–91.
13. T.H. Hwang, J.H. Kim, K.H. Kim, W.J. Moon, and C.Y. Kang: *Met. Mater. Int*., 2014, vol. 20, pp. 13–17.
14. H.M. Chung and O.K. Chopra: *Characterization of Advanced Materials*, Springer, New York, 1990, pp. 123–47.
15. M. Nyström and B. Karlsson: *Mater. Sci. Eng. A*, 1996, vol. 215, pp. 26–38.

16. K.L. Weng, H.R. Chen, and J.R. Yang: *Mater. Sci. Eng. A*, 2004, vol. 379, pp. 119–32.
17. J.K. Sahu: *Effect of 475 °C Embrittlement on the Fatigue Behaviour of a Duplex Stainless Steel*, University of Siegen, Siegen, 2008, p. 131.
18. J.-O. Nilsson: *Mater. Sci. Technol.*, 1992, vol. 8, pp. 685–700.
19. J.-O. Nilsson and P. Liu: *Mater. Sci. Technol.*, 1991, vol. 7, pp. 853–62.
20. A. Mateo, L. Llanes, M. Anglada, A. Redjaimia, and G. Metauer: *J. Mater. Sci.*, 1997, vol. 32, pp. 4533–40.
21. L. Karlsson, L. Ryen, and S. Pak: *Am. Weld. Soc.*, 1995, pp. 28–40.
22. J.J. Shiao, C.H. Tsai, J.H. Huang, and J.J. Kai: *Scr. Mater.*, 1993, vol. 29, pp. 1451–56.
23. A. Redjaïmia and G. Metauer: *J. Mater. Sci.*, 2001, vol. 36, pp. 1717–25.
24. K. Yamamoto, Y. Kimura, and Y. Mishima: *Mater. Trans.*, 2004, vol. 45, pp. 357–60.
25. A. Redjaïmia, A. Proult, P. Donnadieu, and J.P. Morniroli: *J. Mater. Sci.*, 2004, vol. 39, pp. 2371–86.
26. S.-H. Byun, N. Kang, T.-H. Lee, S.-K. Ahn, H.W. Lee, W.-S. Chang, and K.-M. Cho: *Met. Mater. Int.*, 2012, vol. 18, pp. 201–07.
27. A. Redjaimia, P. Ruterana, G. Metauer, and M. Gantois: *Phil. Mag. A*, 1993, vol. 67, pp. 1277–86.
28. C.R Brooks and S.B. Fitch: *Mater. Charact.*, 2000, vol. 45, pp. 365–77.
29. H.M. Chung: Report No. CONF-890215-5, Argonne National Laboratory Materials and Components Technology Division, Argonne, IL, Feb. 1989.
30. H.M. Chung: *Int. J. Press. Vessel Pip.*, 1992, vol. 50, pp. 179–213.
31. O.K. Chopra, H.M. Chung, T.F. Kassner, and W.J. Shack: Report No. ANL/ET/CP—87316 CONF-9510156—11, Argonne National Laboratory, Argonne, IL, Dec. 1995.
32. W. Horvath, W. Prantl, H. Stroißnigg, and E.A. Werner: *Mater. Sci. Eng. A*, 1998, vol. 256, pp. 227–36.
33. M. Ferry: *Encyclopedia of Condensed Matter Physics*, Elsevier, Oxford, 2005, pp. 46–53.
34. L.C.D. Fielding, E.J. Song, D.K. Han, H.K.D.H. Bhadeshia, and D.-W. Suh: *Proceedings of the Royal Society A,* 2014, vol. 470, p. 18.
35. D.L. Engelberg and C. Örnek: *Corr. Eng. Sci. Technol.*, 2014, vol. 49, pp. 535–39.
36. C. Örnek, S. Idris, P. Reccagni, and D. Engelberg: *Metals*, 2016, vol. 6, p. 167.
37. A. Redjaïmia, T. Otarola, and A. Mateo: in *EMC 2008 14th European Microscopy Congress,* Springer, Heidelberg, 2008, pp. 479–80.
38. N. Pettersson, S. Wessman, M. Thuvander, P. Hedström, J. Odqvist, R.F.A. Pettersson, and S. Hertzman: *Mater. Sci. Eng. A*, 2015, vol. 647, pp. 241–48.
39. J.C. de Lacerda, L.C. Cândido, and L.B. Godefroid: *Int. J. Fat.*, 2015, vol. 74, pp. 81–87.
40. Alan Owen Humphreys: *The Low Temperature Fracture Behaviour of the Super Duplex Stainless Steel Zeron 100*, School of Metallurgy and Materials, The University of Birmingham, Birmingham, 1997, p. 220.
41. G. Krauss: *Steels: Processing, Structure, and Performance*, 2nd ed., ASM International, Materials Park, 2015.
42. J. Pilhagen and R. Sandström: *Eng. Fract. Mech.*, 2013, vol. 99, pp. 239–50.
43. T.J. Marrow and C. Harris: *Fat. Fract. Eng. Mater. Struct.*, 1996, vol. 19, pp. 935–47.
44. C. Örnek and D.L. Engelberg: *J. Strain Anal. Eng. Des.*, 2016, vol. 51, pp. 207–19.